



Published in final edited form as:

IEEE Trans Med Imaging. 2011 March ; 30(3): 559–574. doi:10.1109/TMI.2010.2087389.

Mosaic Decomposition: An Electronic Cleansing Method for Inhomogeneously Tagged Regions in Noncathartic CT Colonography

Wenli Cai¹, June-Goo Lee¹, Michael E. Zalis², and Hiroyuki Yoshida¹

¹3D Imaging Research, Department of Radiology, Massachusetts General Hospital and Harvard Medical School, New Chardon Street, Suite 400C, Boston, MA 02114 USA

²Division of Abdominal Imaging & Intervention, Department of Radiology, Massachusetts General Hospital and Harvard Medical School, 55 Fruit Street, Boston, MA 02114 USA

Abstract

Electronic cleansing (EC) is a method that segments fecal material tagged by an X-ray-opaque oral contrast agent in computed tomographic colonography (CTC) images, and effectively removes the material for digitally cleansing the colon. In this study, we developed a novel EC method, called mosaic decomposition (MD), for reduction of the artifacts due to incomplete cleansing of inhomogeneously tagged fecal material in CTC images, especially in noncathartic CTC images. In our approach, the entire colonic region, including the residual fecal regions, was first decomposed into a set of local homogeneous regions, called tiles, after application of a 3-D watershed transform to the CTC images. Each tile was then subjected to a single-class support vector machine (SVM) classifier for soft-tissue discrimination. The feature set of the soft-tissue SVM classifier was selected by a genetic algorithm (GA). A scalar index, called a soft-tissue likelihood, is formulated for differentiation of the soft-tissue tiles from those of other materials. Then, EC based on MD, called MD-cleansing, is performed by first initializing of the level-set front with the classified tagged regions; the front is then evolved by use of a speed function that was designed, based on the soft-tissue index, to reserve the submerged soft-tissue structures while suppressing the residual fecal regions. The performance of the MD-cleansing method was evaluated by use of a phantom and of clinical cases. In the phantom evaluation, our MD-cleansing was trained with the supine (prone) scan and tested on the prone (supine) scan, respectively. In both cases, the sensitivity and specificity of classification were 100%. The average cleansing ratio was 90.6%, and the soft-tissue preservation ratio was 97.6%. In the clinical evaluation, 10 noncathartic CTC cases (20 scans) were collected, and the ground truth of a total of 2095 tiles was established by manual assignment of a material class to each tile. Five cases were randomly selected for training GA/SVM, and the remaining five cases were used for testing. The overall sensitivity and specificity of the proposed classification scheme were 97.1% and 85.3%, respectively, and the accuracy was 94.6%. The area under the ROC curve (A_z) was 0.96. Our results indicated that the use of MD-cleansing substantially improved the effectiveness of our EC method in the reduction of incomplete cleansing artifacts.

Index Terms

Abdominal; computer-aided diagnosis; CT colonography; electronic cleansing; X-ray and CT

I. Introduction

Computed tomographic colonography (CTC), also known as virtual colonoscopy, is a promising technique for noninvasive colon cancer screening that can be an alternative to optical colonoscopy [1], [2]. One of the major obstacles to the wide acceptance of CTC is the need for full cathartic bowel preparation [3], similar to that for conventional optical colonoscopy. In addition to the perceived discomfort and inconvenience associated with full cathartic preparation, which has been identified as one of the major sources of poor patient compliance in colon cancer screening [4]–[7], many studies have warned of potential problems associated with full cathartic preparation, including renal failure, preexisting electrolyte abnormalities, congestive heart failure, ascites, or ileus [8]–[10]. Clinical investigators has been obliged to search for reduced-cathartic or noncathartic methods that can offer patients a well-tolerated and safely performed bowel preparation while providing a sensitivity/specificity similar to that of full cathartic preparation in CTC examination [11]–[13]. *Electronic cleansing* (EC) of the colon is a promising technique for removing the tagged fecal materials in CTC images to “virtually” cleanse the colon after image acquisition.

The early work on EC in CTC dates back to the late 1990s [14]–[16]. The term “electronic cleansing” was first introduced by Wax and Liang at SUNY Stony Brook [14]. However, published work on EC methods has been limited. The model developed by SUNY’s research group classified tagged fluid based on its statistical image features. Chen *et al.* used a Markov random field (MRF) for classification of each voxel by its local feature vector [17]. Li *et al.* reported an improvement by using a hidden MRF to integrate the neighborhood information for removal of nonuniformly tagged fluid [18]. Lately, Wang *et al.* presented a partial volume image segmentation method for classifying voxels that are composed of multiple materials by use of the expectation-maximization (EM) algorithm [19]. Li *et al.* reported the subjective performance of this EM-based method in cleansing of the colon based on 50 cathartic CTC cases [20]. Recently, Wang *et al.* improved their EM-based method by a maximum a *posteriori* expectation-maximization (MAP-EM) algorithm that simultaneously estimates tissue mixture percentages within each voxel and the statistical model parameters for the tissue distribution [21].

Another group of EC methods used an edge model in image segmentation to delineate the tagged regions. Lakare *et al.* used segment rays to analyze the intensity profile as they traverse through the data set for identifying the boundary of tagged fluid [22]. Zalis *et al.* used the Sobel approximation of the image gradient, followed by a dilation operator, to identify the boundaries between air and tagged regions, called air-tagging boundary, and they reported the performance of their method in 68 patients [23]. Serlie *et al.* employed a scale-invariant three-material (air, soft-tissue, and tagged material) transition model to determine the fraction of material in each voxel. They also used the CT values and their gradient magnitude to characterize the boundary between air and tagged fluid [24]. The

subjective performance of their method was later demonstrated in a lesion conspicuity study based on 59 partially or completely submerged polyps and 70 air-exposed polyps [25]. This model was recently extended to the anisotropic point-spread function and sampling near so-called T-junctions, i.e., locations where air-fluid levels hit the colonic wall [26]. Carston *et al.* used a neighborhood voxel-counting method to classify a voxel as stool, tissue, or air [27], and they later expanded their method to combine it with quadratic regression, morphologic operations, and a distance transform [28]. Johnson *et al.* evaluated the performance of this method in 114 noncathartic CTC cases [29]. Although theirs was not strictly an EC method, Franaszek *et al.* used region growing, fuzzy connectedness, and Laplacian level-set methods for removal of tagged fluid to reveal polyps submerged in the tagged regions [30]. Cai *et al.* developed a structure-analysis EC (SA-cleansing) method [31], which employed Hessian response field to enhance the submerged poly-like and fold-like structures while other structures were de-enhanced, and local roughness fields to distinguish thin soft-tissue layer from air-tagging boundaries. SA-cleansing effectively avoids the cleansing artifacts caused by pseudo-enhancement and partial volume effect. However, SA-cleansing cannot avoid the incomplete cleansing artifacts caused by inhomogeneously tagging.

The aforementioned existing EC methods except [28] and [31] were explicitly designed for cathartic fecal tagging CTC, that is, aiming at the removal of tagged fluids, based on the following *EC assumptions*.

- Tagged fluid appears as a bowl-shaped liquid pool located at the bottom of a colonic lumen due to the gravitational effect.
- The air-tagging boundary of tagged fluid is a large, flat, horizontal surface.
- Tagging is homogeneous, i.e., the CT values within the fluid pool are almost constant.

Recent clinical studies showed that fecal tagging and electronic cleansing may increase the diagnostic accuracy of CTC [32]. However, existing EC methods based on the above EC assumptions remain limited in their diagnostic performance in noncathartic CTC, due to the unique features of tagged fecal materials in noncathartic CTC images compared to the tagged fluid in the cathartic CTC images, as demonstrated in Fig. 1.

- *State and homogeneity*: Noncathartic CTC has different states of tagged fecal materials, including those in solid, semi-solid, and liquid state, whereas cathartic CTC has only liquid-state tagged residual fluid. Generally, contrast agents such as iodine are mixed more uniformly in liquid state than in solid state residual fecal materials; thus, non-cathartic CTC presents more inhomogeneously tagged regions than does cathartic CTC.
- *Shape and size*: Due to the flexibility of fluid, the tagged residual fluid in cathartic CTC tends to appear as a bowl-shaped fluid pool at the bottom of a colonic lumen. In contrast, the shape of solid or semi-solid fecal material in non-cathartic CTC tends to be irregular. In addition, the size of the fecal material varies substantially.

- *Distribution*: The tagged residual fluid tends to be located at the bottom of a colonic lumen due to the gravitational effect, whereas solid or semi-solid fecal material in non-cathartic CTC may be distributed anywhere on the colonic wall, even at the ceiling of the colonic lumen against gravity, because of the relatively dry and thus viscous characteristics of the mucosal surface of the colonic wall.

Three major EC artifacts, including soft-tissue degradation, pseudo-soft-tissue structures, and incomplete cleansing, are present in most of the existing EC methods [33]. *Incomplete cleansing* [Fig. 2(b) and (c)], which is caused by the partial removal of only the tagged fecal materials with high CT attenuation, and leaving low-attenuation tagged fecal materials uncleansed, is one of the main artifacts that impair the diagnostic quality of noncathartic CTC [33].

In this study, we developed a novel EC method, called *mosaic decomposition* (MD), for cleansing of inhomogeneously tagged solid or semi-solid fecal materials in noncathartic CTC images for obviating the incomplete cleansing artifacts. The theory behind MD is that an inhomogeneous fecal region can be decomposed into a set of homogeneous subdivisions. Each homogeneous subdivision is composed of one material that can then be identified by classifiers by use of image features of each subdivision. EC is performed by removal of subdivisions that are classified as non-soft-tissue. Thus, precise decomposition and correct classification are two major steps for ensuring the success of MD method.

The remainder of the paper is organized as follows. Section II introduces an overview of *MD-cleansing*, followed by detailed descriptions of two major steps in MD: decomposition and classification. Section III describes the experimental results for assessment of the MD-cleansing method in a colon phantom study and a clinical noncathartic CTC study with a manually established ground truth, and clinical examples of the cleansed non-cathartic CTC images. Sections IV and V present a discussion and conclusions, respectively.

II. Methods

The MD-cleansing method consists of the following four major steps for cleansing of the inhomogeneously tagged regions in CTC images, as illustrated in the diagram in Fig. 3.

1. **Data preparation**: the colonic region including the air-filled lumen and residual fecal regions is first segmented, and then the gradient, Hessian response, and local roughness within the colonic region are calculated.
2. **Tile decomposition**: The entire colonic region is decomposed into a set of local homogeneous subdivisions, called tiles, after application of a 3-D watershed transform to the gradient field.
3. **Tile classification**: Each tile is classified into soft-tissue or nonsoft-tissue by application of a single-class support vector machine (SVM) classifier for soft-tissue discrimination. A scalar index, called a soft-tissue likelihood, is formulated for differentiation of soft-tissue tiles from those of other materials.
4. **Subtraction**: Residual fecal regions are first segmented by use of the level-set method that incorporates the gradient, Hessian response combined with the soft-

tissue index, and local roughness into the speed function terms. The segmented residual fecal regions are replaced by air, followed by a smoothing filter for generating an artificial air-to-soft-tissue mucosal layer between the submerged colonic walls and the replacing air.

In the scope of the paper, the term “tagged fluid” refers to the homogeneously tagged residual fluid, whereas the tagged solid or semi-solid residual fecal material is referred to as “tagged stool.”

A. Data Preparation

In this study, CTC volumetric data were defined in 3-D Euclidean space, R^3 . Let $I(X)$ denote the CT value at a point $X = (x, y, z) \in R^3$ in the CTC volume.

In the step of data preparation, initial colon segmentation was performed by application of a group of alternate region growing methods of air and tagged regions [34]. First, the air-filled colonic lumen is detected by thresholding of -600 HU. Then, each voxel within the 3-D shell of the thresholded colonic air lumen is used as a seed for region growing for segmenting the tagged regions with the threshold of 200 HU. Finally, the entire colonic region is masked by the union of the segmented air regions, the segmented tagged regions, and a 3-D shell thickness of about 10 voxels of the prior segmented air and tagged regions to cover the colonic lumen and wall. After initial colon segmentation, the gradient, Hessian response, and local roughness were calculated at each voxel within the segmented colon region.

The gradient, denoted as $G(X) = |\nabla I(x)| = |(dI/dx, dI/dy, dI/dz)|$, was calculated by the partial first derivatives of a Gaussian function

$$\frac{dI}{dx} = \left[\frac{d}{dx} \text{Gauss}(0; X; \sigma) \right] * I(X) \quad (1)$$

where $\text{Gauss}(0; X; \sigma)$ is an isotropic Gaussian function with a mean value of 0 and a standard deviation of σ , which also serves as the scale in the calculation of partial derivatives. In our experiments, we set $\sigma = 0.8\sigma_0$, where σ_0 is one unit of the voxel size.

We have previously developed the Hessian enhancement functions for folds and polyps to calculate the Hessian response field, and the local roughness function to calculate the local roughness field in [31]. For completeness, we enclose herewith the definitions of the Hessian enhancement functions and local roughness as well as their computing methods.

A Hessian matrix H at point X is defined in

$$H(X) = \begin{pmatrix} \frac{\partial^2 I}{\partial x^2} & \frac{\partial^2 I}{\partial x \partial y} & \frac{\partial^2 I}{\partial x \partial z} \\ \frac{\partial^2 I}{\partial y \partial x} & \frac{\partial^2 I}{\partial y^2} & \frac{\partial^2 I}{\partial y \partial z} \\ \frac{\partial^2 I}{\partial z \partial x} & \frac{\partial^2 I}{\partial z \partial y} & \frac{\partial^2 I}{\partial z^2} \end{pmatrix} \quad (2)$$

where $\frac{\partial^2 I}{\partial x \partial y} = \left[\frac{\partial^2}{\partial x \partial y} \text{Gauss}(0; X; \sigma) \right] * I(X)$.

Let the eigenvalues of Hessian matrix H be λ_1 , λ_2 , and $\lambda_3(|\lambda_1| \quad |\lambda_2| \quad |\lambda_3|)$, and let their corresponding eigenvectors be e_1 , e_2 , and e_3 , respectively. The local morphologic structure of an object can be characterized by use of a combination of the eigenvalues of a Hessian matrix, called *eigenvalue signatures* [35].

Morphologically, folds and polyps submerged in the tagged materials present rut-like (concave ridge) and cup-like (concave cap) shapes, as illustrated in the first column of Table I, because the tagged materials usually have higher CT values than do those for soft-tissue. These two types of structure can be characterized by the eigenvalue signatures of a Hessian matrix and thus can be enhanced by the associated morphological structure enhancement functions, whereas other structures are de-enhanced and subtracted from the CTC images.

The eigenvalue signature and enhancement function of the submerged polyp-like and fold-like structures are illustrated in the second and third columns of Table I, respectively. Fig. 4(e) and (f) demonstrate the submerged polyp-like structure and submerged fold-like structure enhancement image of Fig. 4(d), respectively.

The parameters α , β , and η in F_{rut} and F_{cup} control the scale of the structure that is enhanced, and the parameter γ controls the sharpness of the crest of the fold. The parameters α , β , γ were empirically set to 0.5, 0.3, and 0.3, in order to enhance thin to thick folds ranging from 3 to 10 mm. The parameter η was empirically set to 0.2 to enhance targeted polyps with effective sizes of 5.0 ~ 20.0 mm with a voxel size of 0.7^3 mm^3 in our study.

To reduce the effect of image noise, we formulated a multiscale Hessian response field, $\tilde{H}(x) = \max_{\sigma=\sigma_1}^{\sigma_n} \{F_{\text{cup}}(x; \sigma), F_{\text{rut}}(x; \sigma)\}$, where σ was the scale of the Gaussian function used for calculating the partial second derivatives of the $I(X)$ in the Hessian matrix. The multi-scale Hessian matrix was calculated over two scales in this study, i.e., $0.8\sigma_0$ and $2\sigma_0$. Fig. 4(b) is the Hessian response field of (a), which includes both submerged and nonsubmerged polyp-like and fold-like enhancement functions.

We employed a local roughness analysis that calculates the image smoothness along the periphery of tagged regions in the range of CT values of $0 \text{ HU} \pm 200 \text{ HU}$. This type of smoothness is used for differentiating soft-tissue and the air-tagging boundary caused by the partial volume effect. Local roughness is defined as the sum of the differences between the volumetric curvedness across scales

$$\tilde{R}(X) = \sum_{i=1}^n (B_i \cdot \Delta CV_i^2) \quad (3)$$

where $CV_i = CV_{\sigma_i}(X) - CV_{\sigma_{i-1}}(X)$ represents the difference in the curvedness values at scales i and $i - 1$, n is the number of scales, and B_i is a scale-dependent basis function that weights the difference of the curvedness values at each scale. Here, the local curvedness at voxel X is defined as

$$CV_{\sigma}(X) = \sqrt{\frac{\kappa_{\min}^{\sigma}(X)^2 + \kappa_{\max}^{\sigma}(X)^2}{2}} \quad (4)$$

where $\kappa_{\min}^{\sigma}(X)$ and $\kappa_{\max}^{\sigma}(X)$ are the minimum and maximum principal curvatures at scale σ (i.e., the standard deviation, the same as the scale defined in the Hessian matrix) [23], [24]. The curvedness CV_{σ} is computed by filtering of images with increasing scales, from scale σ_0 to scale $n\sigma_n$, and then, at each scale σ_i , by application of the first and second derivative filters of scale σ_i to the image. In our study, the scale σ_i was selected from 0.5 to 6.0 in voxel units with an interval of 1.0 for calculating of the roughness response. In addition, we used a constant base term, $B_i = 1$ for all scales. Fig. 4(c) is the local roughness field of Fig. 4(a), in which soft-tissue boundaries along the tagged regions are enhanced, whereas the air-tagging boundary is de-enhanced.

B. Tile Decomposition

Suppose that an inhomogeneously tagged region consists of subdivisions of different materials from low to high attenuations on CTC images. A lower attenuation is usually caused by air bubbles and foodstuffs as well as by submerged soft-tissue structures. The purpose in the decomposition is to divide the inhomogeneously tagged regions into local homogeneous tiles by use of a 3-D watershed transform [36], so that each tile represents one homogeneous subdivision composed of one material. The domain of decomposition is the gradient map of CTC images, i.e., $G(X): X \rightarrow R$, is the gradient magnitude at voxel X .

In the context of CTC images, there are two types of tile.

- Large-scale tile: This type of tile is relatively large and has a core of zero gradient, such as large air bubbles, colonic wall, large polyps, and large tagged fluid pools. These tiles can be marked or seeded by the cores of zero gradient.
- Small-scale tile: This type of tile has a relatively small or/and thin region with low contrast, such as submerged folds or polyps, small air bubbles, and undigested foodstuffs. These small/thin regions do not have sufficient cores of zero gradients, such as the submerged fold shown in Fig. 5(d). Incomplete cleansing artifact is mainly caused by this type of tile.

Prior to the watershed transform, tiles are required to be initialized or marked. Large-scale tiles can be marked by use of thresholding of gradient at level g_0 : $T_{g_0} = \{\mathbf{x} \in X | g(\mathbf{x}) \geq g_0\}$. This initialization method may ignore the small-scale tiles due to the low contrast and thus create inhomogeneous tiles, in which one tile contains more than one material, as shown in Fig. 5(a). The submerged thin haustral fold and tagged materials are decomposed into one tile. Generally speaking, small-scale tiles may be initialized by the local minima [37]. However, local minima may introduce over-segmentation, which is typical in the traditional watershed transform, as demonstrated in Fig. 5(b).

We developed a morphological method to initialize small-scale tiles with lower contrast. The following set of rules was employed for initialization of tiles.

- A large-scale tile is initialized by the zero-gradient core using gradient threshold, g_0 .
- A small-scale, polyp-like or fold-like tile submerged in the inhomogeneously tagged regions is initialized by the core of high values from the Hessian response field using threshold, h_0 .

In this study, $g_0 = 0.01$ and $h_0 = 0.5$.

Fig. 5(c) demonstrates the above initialization rules for setting the domain of tiles and the boundaries of the evolved tiles in the example case. We observed that the tagged regions are decomposed into homogeneous tiles, especially the submerged fold and air bubbles. In addition, the number of tiles was reduced significantly. Fig. 5(e) demonstrates the detailed view of tiles initialized by the gradient field, the polyp-like structure enhancement field, and the fold-like structure enhancement field. Nonpolyp-like and nonfold-like structures are enhanced due to their low Hessian response. Fig. 5(f) shows the detailed view of the decomposition result of (e).

C. Tile Classification

The purpose of classification is to determine the material type that composes a tile. Specifically, we used a single-class *support vector machine* (SVM) classifier [38], [39] to determine whether each tile belongs to the soft-tissue class. To attain the optimal performance, an optimization process, called *feature selection*, is performed on the training data sets. The optimal feature set for a classifier is obtained by searching through the possible combinations of features by use of a *genetic algorithm* (GA), which is a stochastic search technique that is based upon the principles of genetic variation and natural selection [40]–[42].

1) Feature Selection—A feature set is modeled as a chromosome $\bar{X} = (x_1, \dots, x_n) \in D^n$, where x_i is the variable (or “gene” in GA terminology), which has a binary value. The search space $D^n \subseteq [0, 1]^n$ is defined as an n -dimensional binary space $x_i \in \{0, 1\}$ ($1 \leq i \leq n$), where 0 and 1 represent the exclusion and inclusion of feature i , respectively. The goal is to find the optimal chromosome (feature set) that maximizes the separation power of a classifier.

The performance of each individual chromosome is evaluated by a *fitness function* $F(\bar{X})$. We formulated the $F(\bar{X})$ by a weighted sum of probability exported by the SVM classifier

$$F(\bar{X}) = \sum_{i=1}^N \text{size}(t_i) \cdot p_i(t_i|\bar{X}) \quad (5)$$

where \bar{X} is the selected feature set, N is the number of tiles in the training data, $\text{size}(t_i)$ is the volumetric size of tile t_i , $p_i(t_i|\bar{X})$ is a conditional function

$$p_i(t_i|\bar{X}) = \begin{cases} P(t_i|\bar{X}), & \text{if tile } t_i \text{ is correctly classified} \\ 1 - P(t_i|\bar{X}), & \text{otherwise} \end{cases} \quad (6)$$

where $P(t_i|X)$ is the probability value of tile t_i exported from the classifier based upon the selected feature set X .

We used five-fold cross validation for calculation of the fitness value for each feature set in the training data. The process of GA evolution was iterated for 100 generations and a population of 10 chromosomes in each generation. After GA selected the resulting optimal feature set X_{opt} , the SVM classifier was finally retrained by use of the entire training data set with the selected optimal feature set X_{opt} .

For the investigation of the optimal feature sets, we have selected a total of 35 features [34], [43].

- CT histogram feature: minimum/maximum, lower/upper,¹ standard deviation, skewness, kurtosis, energy, and entropy.
- CT histogram feature of a core: The core of a tile is defined as a region within a tile in which the gradient at each voxel is below the mean gradient of the tile. The feature set of a core includes the size of core, mean, minimum/maximum, lower/upper, standard deviation, skewness, kurtosis, energy, and entropy.
- Gradient feature: mean and standard deviation of the gradient.
- Gray level co-occurrence matrix feature: including contrast, correlation, and inverse different moment [44].
- Run-length based feature: including short-run emphasis, long-run emphasis, low gray-level-run emphasis, high gray-level-run emphasis, run percentage [45].
- Second-order moment feature: moment invariants J1, J2, and J3 [46].
- Morphological features: including submerged boundary, and mean Hessian response.

Because some features may be correlated, the optimal feature set X_{opt} may not be unique. Therefore, the resulting feature sets may not be the same after individual GA feature selections. The *feature importance* ($w(f_i)$) defines the probability of the feature (f_i) selected by the GA in the final optimal feature set

$$w(f_i) = \frac{\sum_{t=1}^T \text{Selected}(\bar{X}_t | f_i)}{T} \quad (7)$$

where T is the total number of feature selection processes, and \bar{X}_t is the optimal chromosome after a feature selection t . $\text{Selected}(\bar{X}_t | f_i)$ is 1 if feature f_i is selected in \bar{X}_t ; otherwise it is 0.

Numerically, $w(f_i)$ ranges from 0.0 to 1.0. A high importance value indicates that the corresponding feature is selected frequently by the GA, i.e., it plays an important role in the associated classifier.

¹The lower/upper value is defined as the threshold at the left/right side of the peak value in a histogram, which was calculated by the Otsu's thresholding method [54].

Because GA selects the feature set based on the performance of the SVM classifier, GA tends to select the more informative feature if two features are correlated but one is more informative than the other. On the other hand, if two features are highly correlated and have the same information, GA will select either one of them and thus their importance will be split between two features. In this manner, highly correlated features are avoided when we select the feature set by GA. However, the performance of the classifier will not be affected due to the fact that two features are highly correlated and have the same information.

2) Soft-Tissue Classification—A scalar index, called the *soft-tissue likelihood* (L_{ST}), is formulated by use of the probability value exported from the aforementioned soft-tissue SVM classifier for the classification of soft-tissue tiles from other tiles. The L_{ST} index ranges from 0.0 to 1.0, where a high value of the index indicates a high likelihood of soft tissue, whereas a low value indicates a low likelihood of soft-tissue.

Fig. 6 demonstrates the soft-tissue likelihood and the Hessian response field weighted by L_{ST} . In the weighted Hessian response field [Fig. 6(b)], we observe that submerged tiles are selectively enhanced compared to Fig. 4(b), i.e., the tiles that have polyp-like and fold-like structures and are composed of soft-tissue are enhanced, whereas other material tiles are de-enhanced.

The GA and SVM parameters [47] that were used in our feature selection and soft-tissue classification are summarized in Table II.

D. Subtraction

MD-cleansing employed the scheme applied in the SA-cleansing method [31], which employed the Hessian response field (H) to recover the submerged poly-like and fold-like structures. Instead of the Hessian response field (H), MD-cleansing used the Hessian response field weighted by the soft-tissue likelihood ($H \cdot L_{ST}$). We used the level-set method to segment the tagged fecal regions. Level-set is effective in delineating topologically complex and disjointed objects that are difficult to represent by conventional active contour models or snakes [48]–[50]. In addition, level-set can effectively integrate different characterization fields into different speed terms to segment the tagged regions.

The level-set front is initialized by the classified tagged regions, and it is evolved by use of the partial differential equation shown below

$$\frac{\partial \Phi}{\partial t} = \left\{ F(G(X)) - F(\tilde{H}(X) \cdot L_{ST}(X)) - F(\tilde{R}(X)) \right\} \cdot |\nabla \Phi| + C_{\text{curvature}} \nabla \cdot \left(\frac{\nabla \Phi}{|\nabla \Phi|} \right) |\nabla \Phi| \quad (8)$$

where X is a point on the level-set front, F is a speed function, and $C_{\text{curvature}}$ is a parameter controlling the strength of the curvature constraint. We used $C_{\text{curvature}} = 0.2$ in our application.

This evolution equation has three image speed functions: the speed function of gradients $F(G(X))$, which acts as a growing term to expand the tagged regions; the speed function of the Hessian response weighted by L_{ST} , $F(H(X) \cdot L_{ST}(X))$, which acts as a stopping term for

the level-set front at the submerged soft-tissue structures, and the speed function of the local roughness, $F(R(\tilde{X}))$, which acts as a stopping term for the level-set front at the soft-tissue layer. These speed functions are balanced with a mean curvature smoothing constraint [51] in the second term. By use of these speed functions, the level-set front becomes sensitive to submerged soft-tissue structures, whereas it is insensitive to inhomogeneously tagged regions and the air-tagging boundaries. Thus, inhomogeneously tagged regions are segmented and removed along with the air-tagging boundaries, whereas the soft-tissue structures that are submerged in the tagged regions are preserved.

For all of three speed functions, we employed a conventional threshold formulation [52] as defined by (9), because of its flexibility in the selection of the input and its ability to delineate a fuzzy boundary well [53].

$$F(x) = \text{sign}(t(x)) \cdot |t(x)|^n$$

$$\text{where } t(x) = \begin{cases} -1, & \text{if } x < T - \Delta \\ \frac{(x-T)}{\Delta}, & \text{otherwise} \\ 1, & \text{if } x > T + \Delta. \end{cases} \quad (9)$$

Here, $\text{sign}(f)$ is a sign function (also known as an indicator), i.e., 1 if f is positive and -1 if f is negative; n is an integer that controls the smoothness of the speed of the level-set front (we use $n = 2$ for simplicity); T is a threshold value, determined by Otsu's thresholding method [54], which separates the enhanced and non-enhanced objects in the histogram in the shell that is a thick 3-D region encompassing the level-set front [53]. The range, Δ , is set to half of the difference between the threshold and the peak value of the histogram of the enhanced objects. We employed the sparse-field implementation of the level set model [55], in which Φ is represented by the city-block distance. The surface normal and curvature, which require second-order derivative, are calculated by the finite difference derivatives using a $3 \times 3 \times 3$ kernel.

Finally, the tagged regions segmented by the level-set method were replaced with air, and an artificial air-to-soft-tissue transition layer was filled in the boundaries between the submerged colonic walls and the replacing air (subtracted tagged regions) by the mucosa reconstruction method similar to that of [23], followed by an image smoothing filter for reducing the discontinuity between the artificial transition layer and the original soft-tissue layer.

III. Experimental Results

In order to evaluate the cleansing quality of the MD-cleansing method, we designed experiments based on a colon phantom and clinical CTC cases. In each experiment, the results of the MD-cleansing method were compared with those of our previous SA-cleansing method [31].

1) Phantom Experiment

In the phantom experiment, we used a colon phantom (Phantom Laboratory, Salem, NY) made of material that had X-ray attenuation coefficients similar to those of soft-tissue [56].

Twenty-one phantom polyps and eleven phantom folds were embedded in the colon phantom. To simulate the semi-solid fecal materials and the inhomogeneous fecal tagging in noncathartic CTC, we filled the phantom, prior to imaging, with a mixture of aqueous fiber (70 g of psyllium), ground foodstuff (50 g of cereal), and nonionic iodinated agent (1 L of 20 mg/mL concentration of Omnipaque iohexol, GE Healthcare, Milwaukee, WI), the same contrast agent we employed for clinical fecal tagging in CTC.

The colon phantom was scanned by a 64-slice multidetector CT (MDCT) scanner (Siemens Sensation, Erlangen, Germany) twice, once in a native state without tagged material (hereafter called reference phantom) and once filled with the simulating fecal materials (hereafter called fecal-tagging phantom), in both supine and prone positions. The phantom was scanned by use of the following scanning parameters: a reconstruction interval of 0.6 mm, tube current of 40 mA, and voltage of 120 kVp. CT images obtained from the reference phantom served as a reference standard, and those from the fecal-tagging phantom were used for evaluation of the MD- and SA-cleansing methods. Because the phantom was removed from the CT table while it was filled with tagged material, the fecal-tagging phantom was registered rigidly to the reference phantom by use of a 3-D rigid-body transformation [57].

A total of 209 and 152 tiles were generated in supine and prone CTC images of the fecal-tagging phantom, respectively. Each tile in the fecal-tagging phantom was mapped to a tile in the reference phantom, called a reference tile. 152 out of 209 and 82 out of 152 tiles were identified as soft-tissue tiles in the supine and prone images, respectively. Other tiles were identified as nonsoft-tissue tiles, i.e., air or fecal-tagging tiles.

Fig. 7(a) and (d) shows one of the coronal and axial CTC images of the fecal-tagging phantom. Fig. 7(b) and (e) are their corresponding gradient images. These images demonstrate that the tagged materials are inhomogeneously mixed with air bubbles and foodstuff. Fig. 7(c) and (f) shows the tiles decomposed based on our morphological marker-initialization method by use of the gradient and Hessian response field. The major components, including the colon wall, lumen air, submerged folds and polyps, as well as air bubbles and foodstuffs, were clearly decomposed.

The supine/prone and prone/supine combinations were employed for the training/testing of the GA feature selection and the SVM classifier. In the GA feature selection, the average fitness value of the optimal feature set was 0.968. In both supine/prone and prone/supine experiments, the SVM classifier that was finally trained by the optimal feature set yielded a 100% sensitivity and 100% specificity in the testing data. Fig. 8 compares the 2-D and 3-D images of the cleansed phantom with the reference phantom.

For the purpose of evaluation of the cleansing quality, we divided the reference phantom into 10 segments along the center-line of the lumen, as illustrated in Fig. 9(a). The air lumen in the reference phantom was classified by the thresholding function D_{air}

$$D_{\text{air}}(\mathbf{x}) = \begin{cases} 1, & \text{if } I(\mathbf{x}) < -600HU \\ 0, & \text{otherwise.} \end{cases} \quad (10)$$

The tagging mask (M_{tagging}) in (11) was defined as the regions of the air lumen in the reference phantom that were covered by the tagged materials in the fecal-tagging phantom

$$M_{\text{tagging}} = \{\forall \mathbf{x}, \mathbf{x} \in M_{\text{colon}} | D_{\text{air}}(\mathbf{x} | I_{\text{reference}}) = 1 \cap D_{\text{air}}(\mathbf{x} | I_{\text{tagging}}) = 0\} \quad (11)$$

where M_{colon} is the segmented colon mask, which is the thick colonic wall that was segmented in the first step of data preparation, $I_{\text{reference}}$ and I_{tagging} are CTC images of the reference phantom and the fecal-tagging phantom, respectively.

Thus, the cleansing ratio ($R_{\text{cleansing}}$) is defined as the ratio of the number of voxels in the tagging mask that was cleansed, i.e., became air voxels, in the cleansed phantom (I_{EC}), to the total number of voxels in the tagging mask

$$R_{\text{cleansing}} = \frac{\text{Size}\{\forall \mathbf{x}, \mathbf{x} \in I_{\text{tagging}} | D_{\text{air}}(\mathbf{x} | I_{\text{EC}}) = 1\}}{\text{Size}\{M_{\text{tagging}}\}} \times 100\%. \quad (12)$$

In a similar manner, we can define the soft-tissue mask (M_{ST}) and the ratio of soft-tissue preservation (R_{ST})

$$\begin{aligned} M_{\text{ST}} &= \{\forall \mathbf{x}, \mathbf{x} \in M_{\text{colon}} | D_{\text{air}}(\mathbf{x} | I_{\text{reference}}) = 0\} \\ R_{\text{ST}} &= \frac{\text{Size}\{\forall \mathbf{x}, \mathbf{x} \in M_{\text{ST}} | D_{\text{air}}(\mathbf{x} | I_{\text{EC}}) = 0\}}{\text{Size}\{M_{\text{ST}}\}} \times 100\%. \end{aligned} \quad (13)$$

Table III lists the mean values of the cleansing ratio and soft-tissue preservation ratio in 10 segments of the phantom. Fig. 9(b)–(d) shows the fifth segment: the reference, the SA-cleansing, and the MD-cleansing results, respectively, which demonstrates that the MD-cleansing removes the inhomogeneously tagged region while preserving the soft-tissue.

2) Clinical Experiment

We applied our MD-cleansing method to the clinical fecal-tagging CTC cases with non-cathartic bowel preparation. Patients underwent a 48-h bowel preparation with a low-fiber, low-residue diet, oral administration of 7.5 ml (300 mg/ml concentration of Omnipaque iohexol, GE Healthcare, Milwaukee, WI) nonionic iodine diluted in 300 ml at each of six meals, and 30 ml Omnipaque diluted in 960 ml water in the morning of the CTC examination. No cathartic agent was used in the bowel preparation. MDCT scanning (LightSpeed; GE Medical Systems, Milwaukee, WI) was performed in both supine and prone positions. It should be noted that, unlike the cathartic CTC cases, most of the tagged materials in these noncathartic cases were semi-fluid/solid with inhomogeneous tagging rather than fluid with homogeneous tagging, and thus these were difficult cases for EC.

A total of 10 noncathartic CTC cases (20 scans) were collected, among which each case contained at least one polyp ≥ 6 mm. In these 10 cases, there were a total of 15 polyps ≥ 6 mm, including nine polyps 6 ~ 8 mm, three polyps 8 ~ 10 mm, and three polyps ≥ 10 mm.

A total of 2095 tiles were decomposed in the 20 scans, in which the median number of tiles per scan was 115, the minimum number was 49, and the maximum number was 196. The decomposition images such as Fig. 5(c) and a list of tiles were exported to a Viatronix Workstation (Viatronix. Inc., Stony Brook, NY) and were visually assessed by a radiology fellow and an experienced radiologist. The reference standard was established by manual assignment of a material class to each tile after review of the 2-D axial images. There were 1403 tiles assigned as soft-tissue; the others were nonsoft-tissue tiles.

Of the 10 cases collected, five cases (10 scans/955 tiles/571 soft-tissue tiles) were randomly selected for training of GA/SVM, and the remaining five cases (10 scans/1160 tiles/832 soft-tissue tiles) were used for evaluation. We tested the GA feature selection 100 times on the training data. Fig. 10 shows the importance map of the 35 features selected for soft-tissue classification. The minimum, maximum, and average fitness value were 0.963, 0.968, and 0.965, respectively. This indicated that the performance of GA was stable in selecting an optimal feature set.

After GA feature selection, we selected the optimal feature set with the maximum fitness value, i.e., 0.968, which is listed in Table IV, and the SVM classifier was finally trained with the optimal feature set and the entire training data set before evaluation.

Fig. 11 illustrates the overall performance of the SVM classifier, which is represented by the receiver operating characteristic (ROC) curve and the accuracy curve. The area under the ROC curve (A_z) was 0.96. At the operating point of 0.7, the sensitivity and specificity of the SVM classifier was 97.1% and 85.3%, respectively, and the accuracy $[(TP + TN)/(\text{total number of tiles})]$ was 94.6%.

Visual assessment was also performed for evaluating the cleansing quality. There were seven polyps in the five testing cases. Visual assessment confirmed that all polyps in the testing cases were classified as soft-tissue at the aforementioned L_{ST} operating point of 0.7. Thus, they were clearly preserved in the resulting cleansed images.

Fig. 12 shows a fecal-tagging CTC case and its cleansed images after the application of MD-cleansing and SA-cleansing, respectively. Fig. 12(b) and (e) shows the reduction of incomplete cleansing artifacts by MD-cleansing, whereas Fig. 12(c) and (f) shows that of SA-cleansing. Visual comparison indicates that MD-cleansing reduced the incomplete cleansing artifacts much better than did SA-cleansing. More-over, MD-cleansing preserved the thin haustral fold submerged in the inhomogeneously tagged stool. Fig. 13 compares the 3-D endoluminal views of the submerged fold that is pointed out by the white arrow in Fig. 12(a) in MD-cleansing and SA-cleansing. We observed that the inhomogeneously tagged stool was clearly cleansed by MD-cleansing.

Fig. 14 demonstrates more clinical examples of the MD-cleansing in the cleansing of inhomogeneously tagged stool: the semi-solid stool was cleansed, whereas the submerged folds were well preserved.

IV. Discussion

In the phantom experiment, we observed that the inhomogeneously tagged materials were completely cleansed. However, the cleansing ratio was approximately 91%. The remaining un-cleansed region was a thin layer of contrast agent that was adherent to the dry and viscous mucosal surface of the colonic wall. This thin layer has a thickness of only about 1–2 voxels. It is unique to noncathartic CTC, as shown in Fig. 15(a) and (c), which show the difference between the reference phantom and the cleansed phantom within the air mask.

Because most soft-tissue is far from the colon, the accuracy of soft-tissue preservation would be irrelevant if we included the entire images. Thus, the soft-tissue mask (M_{ST}) that we used for the estimation of the ratio of soft-tissue preservation (R_{ST}) is a thick colonic wall (M_{colon}) that was segmented in the first step, which has a thickness of about 10 voxels. If the criterion for R_{ST} is 100%, the EC performance is assessed by how different R_{ST} is from 100%. SA-cleansing missed 1% of the soft-tissue, whereas MD-cleansing missed 2.4% of the soft-tissue in the mask. This difference was mainly caused by the watershed transform, which equally divided the boundaries between soft-tissue and tagged material. At the boundaries between the soft-tissue and residual fecal regions, tiles that were classified as tagged fluid or stool may contain a very thin layer that mixed with a small quantity of soft-tissue, as shown in Fig. 15(b) and (d), which show the difference between the reference phantom and cleansed phantom within the soft-tissue mask. This is the main reason why SA-cleansing had a slightly better ratio of soft-tissue preservation than did MD-cleansing.

Because we replaced the entire segmented tagged region with air, an artificial layer of mucosa was generated at the boundaries between the submerged colonic wall and the filled air (subtracted regions) after subtraction. For reduction of the possible discontinuity between the artificial mucosa layer and the original soft-tissue in the colonic wall, a Gaussian smoothing filter was applied to these regions. This may cause a fuzzy appearance of the submerged colonic wall after subtraction in cleansed images.

One limitation of the study is the relatively large number of soft-tissue tiles in the training and testing data. This is partially caused by our tile initialization method. We employed Hessian response fields to place markers for segmentation of small objects with low contrast. The nonpolyp-like and nonfold-like structures were de-enhanced by the Hessian response field and thus were filtered out as part of the tagging background. Large tiles including the air lumen, colonic soft-tissue portion, and tagging background are easily identified. MD was designed to reducing incomplete cleansing artifacts and thus was applied to tiles of small size. However, the small number of nonsoft-tissue tiles may cause biased performance of the SVM classifier. We will evaluate this issue in a large clinical evaluation in the future.

Although the artifact of incomplete cleansing, which is caused by inhomogeneity in tagging, is seen less commonly with cathartic bowel preparations, it is one of the major artifacts that

impair the diagnostic quality of reduced and noncathartic bowel preparations in CTC. Li *et al.* [18] suggested using a hidden Markov random field (MRF) to integrate the neighborhood information for overcoming the nonuniformity problems. The hidden MRF was designed to solve the nonuniformity caused by random noise. However, artifacts of incomplete cleansing are caused mainly by structural noise such as air bubbles, fats, and undigested foodstuffs, which are a different type of inhomogeneity from that of the nonuniform distribution of the contrast agent. The method proposed by Li *et al.* was not designed for removal of this type of artifact. The SA-cleansing method previously developed by Cai *et al.* [31] cannot avoid completely the structural noise in the inhomogeneously tagged region, such as small foodstuffs or air bubbles that have rut-like and cup-like shapes. In the noncathartic CTC study performed by Johnson *et al.* [29], which employed the cleansing method developed by Carston *et al.* [27], [28], more than half of the cases showed the incomplete cleansing artifacts, including islands of residual stool and residual halos. In their study, a 3-D fly-through was not possible because of the cleansing artifacts. Some authors tried to remove floating-island-like structures with an ad hoc method [58]. The MD-cleansing method provides a solution to the removal of the structural noise in inhomogeneous tagging for cleansing of the inhomogeneously tagged regions. The feature importance map in Fig. 10 provides information as to what image features may be employed for detecting and segmenting of inhomogeneously tagged regions.

Another limitation of the MD-cleansing method is that the optimal feature set selected by GA may vary for different bowel preparations. Thus, we need to manually establish a reference standard for each bowel preparation for effective training of the GA/SVM classifier, which is a tedious and time-consuming task. Once we establish the reference standard of soft-tissue tiles, MD-cleansing can be trained to effectively cleanse the tagged fecal materials. Hence, another future work is to identify the common salient feature set for different noncathartic bowel preparations. Although the regimes for noncathartic bowel preparation may vary across different clinical protocols, we observed that the image features on CTC are similar. Thus, we will first minimize the feature set by identifying and merging the correlated features, and then finding the common salient features by comparing the importance maps from different bowel preparations. With a common salient feature set for noncathartic CTC, the workload of manually establishing of reference standard will be minimized.

In addition, the computational cost of MD-cleansing method is relatively high. It takes approximately 30 min to cleanse the CTC images electronically from a scan of a patient on a standard PC. Optimization and parallelization of the EC code is under way.

V. Conclusion and Future Work

Incomplete cleansing artifact is the main technical barrier to applying noncathartic CTC in clinical practice, because of the lack of an effective method for electronic cleansing of the inhomogeneously tagged fecal materials. This paper has presented a novel EC method, called mosaic decomposition, which is designed to reduce incomplete cleansing artifacts in CTC, especially in non-cathartic CTC images. Unlike existing EC methods, our method subtracts a tagged region by use of soft-tissue likelihood. Evaluation of results based on

phantom and clinical cases showed that the MD-cleansing method improved the cleansing ratio of the tagged fecal residues compared to our previously reported cleansing method, and thus the MD-cleansing method was able to effectively remove the artifacts of incomplete cleansing.

This paper presents the technical aspects of MD-cleansing. We are currently performing a clinical analysis of the improvement of each artifact in clinical noncathartic CTC cases. Thus, a clinical study for a quantitative clinical evaluation of EC artifacts by use of MD-cleansing and the parallelization of MD-cleansing are the major future work of this study.

Acknowledgments

This work was supported in part by Cancer Prevent Foundation Research Grant, NIH/NCI grants R01CA095279 (PI: Yoshida) and R01CA131718 (PI: Yoshida) from the U.S. Public Health Service, and the American Cancer Society under Research Scholar Grant RSG-05-088-01-CCE (PI: Yoshida).

The authors would like to thank the reviewers for the valuable comments and E. Lanzl for language editing and proofreading of the manuscript.

References

1. Morrin MM, LaMont JT. Screening virtual colonoscopy—Ready for prime time? *N Engl J Med*. Dec.2003 349:2261–2264. [PubMed: 14657435]
2. Levin B, Brooks D, Smith RA, Stone A. Emerging technologies in screening for colorectal cancer: CT colonography, immunochemical fecal occult blood tests, and stool screening using molecular markers. *CA Cancer J Clin*. Jan-Feb;2003 53:44–55. [PubMed: 12568443]
3. Elwood JM, Ali G, Schlup MM, McNoe B, Barbezat GO, North F, Sutton K, Parry B, Chadwick VS. Flexible sigmoidoscopy or colonoscopy for colorectal screening: A randomized trial of performance and acceptability. *Cancer Detect Prev*. 1995; 19:337–347. [PubMed: 7553676]
4. Ristvedt SL, McFarland EG, Weinstock LB, Thyssen EP. Patient preferences for CT colonography, conventional colonoscopy, and bowel preparation. *Am J Gastroenterol*. Mar.2003 98:578–585. [PubMed: 12650790]
5. Wardle J, Sutton S, Williamson S, Taylor T, McCaffery K, Cuzick J, Hart A, Atkin W. Psychosocial influences on older adults' interest in participating in bowel cancer screening. *Prev Med*. Oct.2000 31:323–334. [PubMed: 11006057]
6. Weitzman ER, Zapka J, Estabrook B, Goins KV. Risk and reluctance: Understanding impediments to colorectal cancer screening. *Prev Med*. Jun.2001 32:502–513. [PubMed: 11394954]
7. Gluecker TM, Johnson CD, Harmsen WS, Offord KP, Harris AM, Wilson LA, Ahlquist DA. Colorectal cancer screening with CT colonography, colonoscopy, and double-contrast barium enema examination: Prospective assessment of patient perceptions and preferences. *Radiology*. May.2003 227:378–384. [PubMed: 12732696]
8. Clarkston WK, Tsen TN, Dies DF, Schratz CL, Vaswani SK, Bjerregaard P. Oral sodium phosphate versus sulfate-free polyethylene glycol electrolyte lavage solution in outpatient preparation for colonoscopy: A prospective comparison. *Gastrointest Endosc*. Jan; 1996 43(1):42–48. [PubMed: 8903817]
9. Orias M, Mahnensmith RL, Perazella MA. Extreme hyperphosphatemia and acute renal failure after a phosphorus-containing bowel regimen. *Am J Nephrol*. Jan; 1999 19(1):60–63. [PubMed: 10085452]
10. Beloosesky Y, Grinblat J, Weiss A, Grosman B, Gafter U, Chagnac A. Electrolyte disorders following oral sodium phosphate administration for bowel cleansing in elderly patients. *Arch Intern Med*. Apr; 2003 163(7):803–808. [PubMed: 12695271]
11. Lefere P, Gryspeerdt S, Baekelandt M, Van Holsbeeck B. Laxative-free CT colonography. *AJR Am J Roentgenol*. Oct.2004 183:945–948. [PubMed: 15385285]

12. Iannaccone R, Laghi A, Catalano C, Mangiapane F, Lamazza A, Schillaci A, Sinibaldi G, Murakami T, Sammartino P, Hori M, Piacentini F, Nofroni I, Stipa V, Passariello R. Computed tomographic colonography without cathartic preparation for the detection of colorectal polyps. *Gastroenterology*. Nov.2004 127:1300–1311. [PubMed: 15520999]
13. Johnson KT, Carston MJ, Wentz RJ, Manduca A, Anderson SM, Johnson CD. Development of a cathartic-free colorectal cancer screening test using virtual colonoscopy: A feasibility study. *AJR Am J Roentgenol*. Jan.2007 188:W29–36. [PubMed: 17179324]
14. Wax, M.; Liang, Z.; Chiou, R.; Kaufman, A.; Viswambharan, A. Electronic colon cleansing for virtual colonoscopy. *Proc. 1st Symp. Virtual Colonoscopy; Boston, MA. 1998; p. 94-94.*
15. Liang, Z.; Yang, F.; Wax, M.; Li, J.; You, J.; Kaufman, A.; Hong, L.; Li, H.; Viswambharan, A. Inclusion of a priori information in segmentation of colon lumen for 3-D virtual colonoscopy. *IEEE Nucl. Sci. Soc. Med. Imag. Conf; Albuquerque, NM. 1997; p. 1423-1427.*
16. Liang, Z.; Chen, D.; Chiou, R.; Li, B.; Kaufman, A.; Wax, M.; Viswambharan, A. On segmentation of colon lumen for virtual colonoscopy. *SPIE Med. Imag.; San Diego, CA. 1999; p. 270-278.*
17. Chen D, Liang Z, Wax MR, Li L, Li B, Kaufman AE. A novel approach to extract colon lumen from CT images for virtual colonoscopy. *IEEE Trans Med Imag*. Dec; 2000 19(12):1220–1226.
18. Li, L.; Chen, D.; Lakare, S.; Kreeger, K.; Bitter, I.; Kaufman, A.; Wax, M.; Djunic, P.; Liang, Z. An image segmentation approach to extract colon lumen through colonic material tagging and hidden Markov random field model for virtual colonoscopy. *SPIE Med. Imag.; San Diego, CA. 2002; p. 406-411.*
19. Wang Z, Liang Z, Li X, Li L, Li B, Eremina D, Lu H. An improved electronic colon cleansing method for detection of colonic polyps by virtual colonoscopy. *IEEE Trans Biomed Eng*. Aug; 2006 53(8):1635–1646. [PubMed: 16916098]
20. Li, L.; Wang, S.; Wang, Z.; Wang, J.; Lu, H.; Liang, Z. Gain by mixture-based image segmentation for virtual colonoscopy with colonic material tagging. *Med. Imag. 2007: Physiol., Function, Structure from Medical Images; San Diego. 2007; p. 65110V-1-65110V-10.*
21. Wang S, Li L, Cohen H, Mankes S, Chen JJ, Liang Z. An EM approach to MAP solution of segmenting tissue mixture percentages with application to CT-based virtual colonoscopy. *Med Phys*. Dec.2008 35:5787–5798. [PubMed: 19175136]
22. Lakare, S.; Chen, D.; Li, L.; Kaufman, A.; Liang, Z. Electronic colon cleansing using segmentation rays for virtual colonoscopy. *SPIE Med. Imag.; San Diego. 2002; p. 412-418.*
23. Zalis ME, Perumpillichira J, Hahn PF. Digital subtraction bowel cleansing for CT colonography using morphological and linear filtration methods. *IEEE Trans Med Imag*. Nov; 2004 23(11): 1335–1343.
24. Serlie, IW.; Truyen, R.; Florie, J.; Post, F.; van Vliet, L.; Vos, FM. Computed cleansing for virtual colonoscopy using a three-material transition model. *Proc. MICCAI; Montreal, Canada. 2003; p. 175-183.*
25. Serlie IW, de Vries AH, van Vliet LJ, Nio CY, Truyen R, Stoker J, Vos FM. Lesion conspicuity and efficiency of CT colonography with electronic cleansing based on a three-material transition model. *AJR Am J Roentgenol*. 2008; 191:1493–1499. [PubMed: 18941091]
26. Serlie I, Vos F, Truyen R, Post F, Stoker J, van Vliet L. Electronic cleansing for CT colonography using a scale invariant three material model. *IEEE Trans Biomed Eng*. Jun; 2010 57(6):1306–1317. [PubMed: 20172789]
27. Carston, MJ.; Wentz, RJ.; Manduca, A.; Johnson, D. CT colonography of the unprepraed colon: An evaluation of electronic stool subtraction. *Medical Imag.2005: Physiol., Function, Structure from Medical Images; San Diego. 2005; p. 424-431.*
28. Carston, MJ.; Manduca, A.; Johnson, D. Electornic stool subtraction using quadratic regression, morphological operations, and distance transform. *Med. Imag. 2007: Physiology, Function, and Structure from Medical Images; San Diego. 2007; p. 6511W-1-6511W-12.*
29. Johnson CD, Manduca A, Fletcher JG, MacCarty RL, Carston MJ, Harmsen WS, Mandrekar JN. Noncathartic CT colonography with stool tagging: Performance with and without electronic stool subtraction. *AJR Am J Roentgenol*. Feb.2008 190:361–366. [PubMed: 18212221]

30. Franaszek M, Summers RM, Pickhardt PJ, Choi JR. Hybrid segmentation of colon filled with air and opacified fluid for CT colonography. *IEEE Trans Med Imag.* Mar; 2006 25(3):358–368.
31. Cai W, Zalis ME, Näppi J, Harris GJ, Yoshida H. Structure-analysis method for electronic cleansing in cathartic and noncathartic CT colonography. *Med Phys.* Jul.2008 35:3259–3277. [PubMed: 18697551]
32. Pickhardt PJ, Choi JH. Electronic cleansing and stool tagging in CT colonography: Advantages and pitfalls with primary three-dimensional evaluation. *AJR Am J Roentgenol.* Sep.2003 181:799–805. [PubMed: 12933484]
33. Cai W, Yoshida H, Zalis ME, Nappi JJ, Harris GJ. Informatics in radiology: Electronic cleansing for non-cathartic CT colonography: A structure-analysis scheme. *Radiographics.* Mar 10.2010
34. Russ, JC. The image processing handbook. 2007. [Online]. Available: <http://www.loc.gov/catdir/enhancements/fy0662/2006040469-d.html>
35. Sato Y, Westin C, Bhalerao A, Nakajima S, Shiraga N, Tamura S, Kikinis R. Tissue classification based on 3-D local intensity structures for volume rendering. *IEEE Trans Vis Comput Graphics.* Apr-Jun;2000 6(2):160–180.
36. Najman L, Couprie M, Bertrand G. Watersheds, mosaics, and the emergence paradigm. *Discrete Applied Mathematics.* 2005; 147:301–324.
37. Dougherty, ER. An Introduction to Morphological Image Processing. Society of Photo-optical Instrumentation Engineers; 1992.
38. Weston, J.; Watkins, C. Multi-class support vector machines. Department of Computer Science, Royal Holloway; Egham, U.K: Univ. London; 1998.
39. Vapnik, VN. The Nature of Statistical Learning Theory. New York: Springer; 2000.
40. Anastasio MA, Yoshida H, Nagel R, Nishikawa RM, Doi K. A genetic algorithm-based method for optimizing the performance of a computer-aided diagnosis scheme for detection of clustered micro-calcifications in mammograms. *Med Phys.* 1998; 25:1613–1620. [PubMed: 9775365]
41. Goldberg, GE. Genetic Algorithms in Search, Optimization, and Machine Learning. Reading, MA: Addison-Wesley; 1989.
42. Yoshida, H.; Anastasio, A.; Nagel, R.; Nishikawa, R.; Doi, K. Computer-aided diagnosis for detection of clustered microcalcifications in mammograms: Automated optimization of performance based on genetic algorithm. In: Doi, K.; MacMahon, H.; Giger, ML.; Hoffmann, KR., editors. *Computer-Aided Diagnosis in Medical Imaging.* New York: Elsevier; 1999. p. 247-252.
43. Materka A, Strzelecki M. Texture analysis methods—A review. Tech Univ Lodz, Inst Electron, COST B11 Rep. 1998 COST B11 report.
44. Xu Y, van Beek EJ, Hwanjo Y, Guo J, McLennan G, Hoffman EA. Computer-aided classification of interstitial lung diseases via MDCT: 3-D adaptive multiple feature method (3-D AMFM). *Acad Radiol.* Aug.2006 13:969–978. [PubMed: 16843849]
45. Sonka, M.; Hlavac, V.; Boyle, R. *Image Processing, Analysis, and Machine Vision.* 3. Melbourne, Australia: Cengage; 2007.
46. Sadjadi FA, Hall EL. Three-dimensional moment invariants. *IEEE Trans Pattern Anal Mach Intell.* Mar; 1980 2(2):127–136. [PubMed: 21868883]
47. Lin, C. LIBSVM: An integrated software for support vector classification and regression. 2000. [Online]. Available: <http://www.csie.ntu.edu.tw/~cjlin/libsvm>
48. Osher S, Sethian J. Fronts propagating with curvature-dependent speed: Algorithms based on Hamilton-Jacobi formulations. *J Computat Phys.* 1988; 79:12–49.
49. Sethian, JA. *Level Set Methods and Fast Marching Methods: Evolving Interfaces in Computational Geometry, Fluid Mechanics, Computer Vision, and Materials Science.* 2. Cambridge, U.K: Cambridge Univ. Press; 1999.
50. Osher, S.; Fedkiw, R. *Level Set Methods and Dynamic Implicit Surface.* New York: Springer-Verlag; 2002.
51. Ho, S.; Bullitt, E.; Gerig, G. Level set evolution with region competition: Automatic 3-D segmentation of brain tumors. *Proc. 16th Int. Conf. Pattern Recognit;* 2002; p. 532-535.
52. Sethian, J. *Level Set Methods: Evolving Interfaces in Geometry, Fluid Mechanics, Computer Vision and Material Sciences.* Cambridge, U.K: Cambridge Univ. Press; 1996.

53. Cai W, Holalkere N, Harris G, Sahani D, Yoshida H. Dynamic-threshold level set method for volumetry of porcine kidney in CT images: In-vivo and ex-vivo assessment of the accuracy of volume measurement. *Acad Radiol.* 2007; 14:890–896. [PubMed: 17574138]
54. Otsu N. A threshold selection method from gray level histograms. *IEEE Trans Syst Man Cybern.* 1979; 9:62–66.
55. Whitaker RT. A level-set approach to 3-D reconstruction from range data. *Int J Comput Vis.* 1998; 29:203–231.
56. Zalis ME, Perumpillichira JJ, Kim JY, Frate CD, Magee C, Hahn PF. Polyp size at CT colonography after electronic subtraction cleansing in an anthropomorphic colon phantom. *Radiology.* Jul.2005 236:118–124. [PubMed: 15987967]
57. Thévenaz P, Unser M. A pyramid approach to subpixel registration based on intensity. *IEEE Trans Image Process.* Jan; 1998 7(1):27–41. [PubMed: 18267377]
58. Guendel L, Suehling M, Eckert H. Novel method for digital subtraction of tagged stool in virtual colonoscopy. *SPIE Med Imag.* 2008:6914 C-1–6914 C-6.

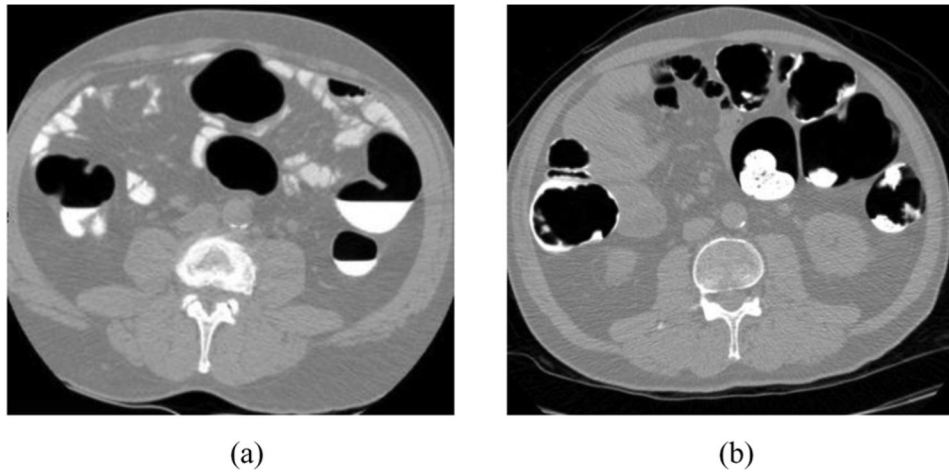


Fig. 1.

(a) Cathartic bowel preparation tends to generate a bowl-shaped fluid pool with a uniform CT value. (b) In noncathartic bowel preparation, tagged fecal material often appears as a semi-solid fecal material consisting of mixtures of air bubbles, fat, undigested foodstuffs, and unevenly distributed contrast agents.

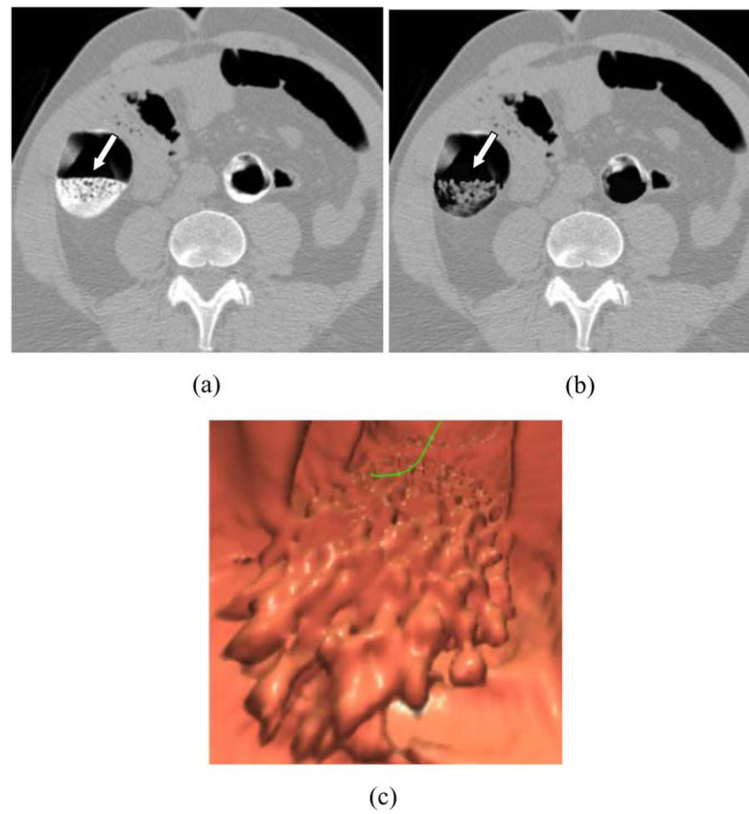


Fig. 2. Inhomogeneous tagging and incomplete cleansing artifact. (a) Inhomogeneously tagged region in a noncathartic CTC case. (b) Incomplete cleansing artifacts, caused by the partial removal of only the tagged fecal materials with high CT attenuation, and leaving low-attenuation tagged fecal materials un-cleansed. (c) Endoluminal view of the artifacts of incomplete cleansing.

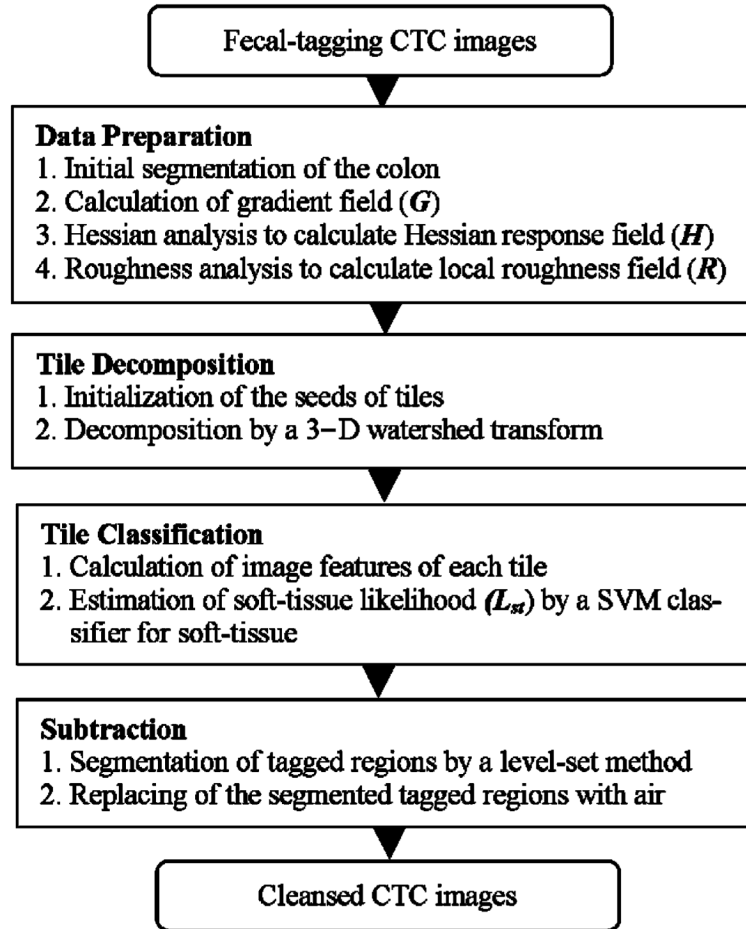


Fig. 3. Diagram of MD-cleansing scheme for noncathartic CTC images. Each box represents a process (bold headers) and the steps in the process.

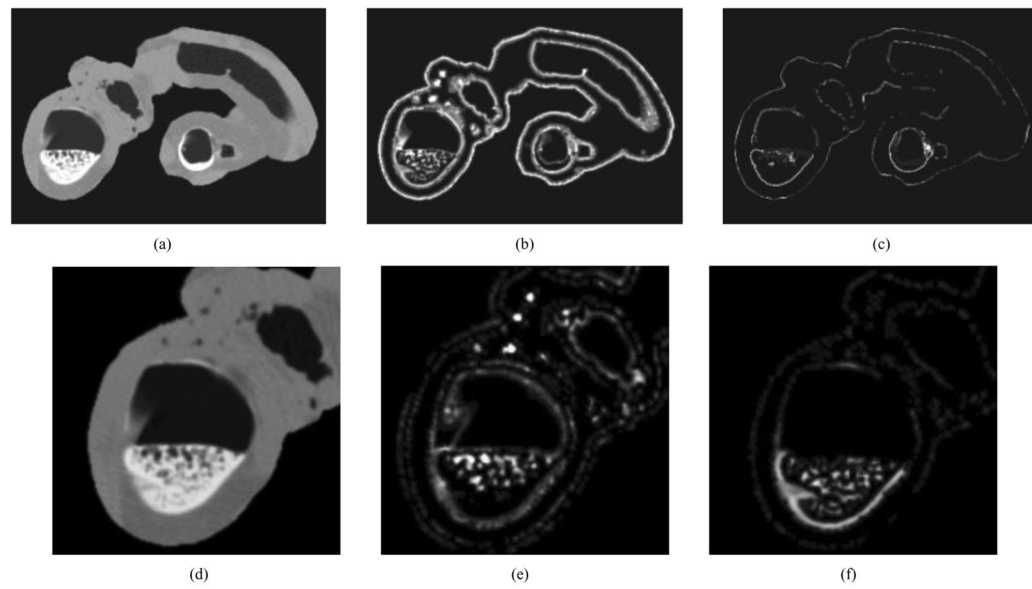


Fig. 4. Demonstration of data preparation. (a) One axial image of a segmented colon in a noncathartic CTC case. (b) The polyp-like and fold-like structure Hessian response image of (a). (c) The roughness response image of (a). (d) Detailed view of the inhomogeneously tagged region in (a). (e) Polyp-like structure enhancement image of (d). (f) Fold-like structure enhancement image of (d).

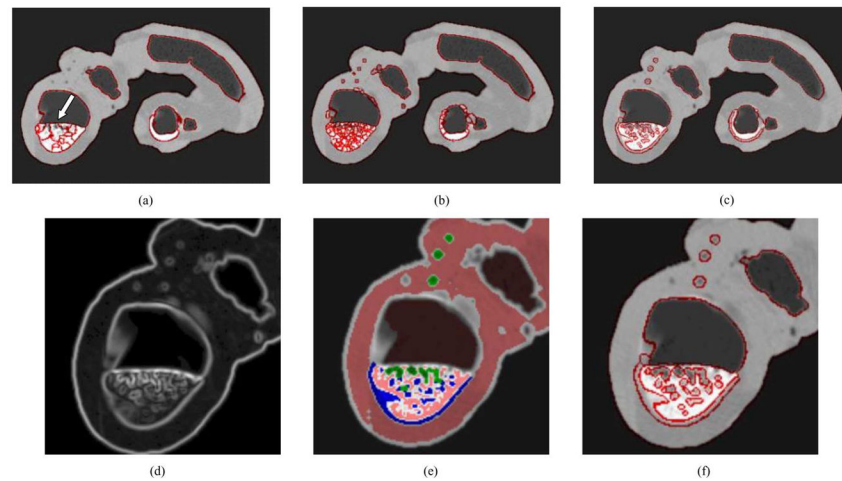


Fig. 5. Decomposition in the inhomogeneously tagged region. (a) Decomposition with markers placed by zero-gradient only created large tiles (85 tiles in this case). It fails to create homogenous tiles: the submerged fold is mixed with tagged materials in one tile. (b) Decomposition with markers placed by zero-gradient and minimum points generates a large number of tiles (7324 tiles). (c) Decomposition with markers placed by zero-gradient and Hessian response creates homogenous tiles with a smaller number of tiles (135 tiles). (d) Detailed view of the gradient image of the inhomogeneously tagged region in (a). (e) Markers are placed by use of gradient (pink), fold-like structure enhancement field (blue), and polyp-like structure enhancement field (green). (f) Decomposition results of (e).

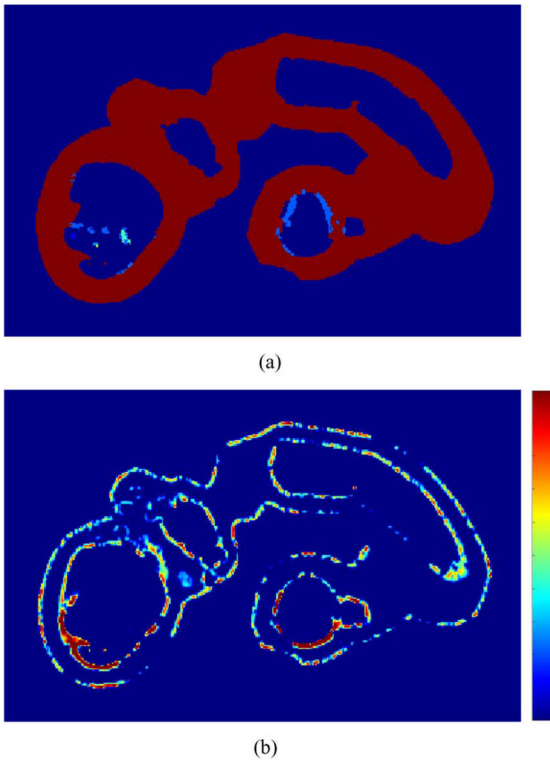


Fig. 6. (a) Soft-tissue likelihood of Fig. 4(a) generated by the SVM classifier. (b) Hessian response field weighted by the soft-tissue likelihood Fig. 4(b) \times Fig. 6(a).

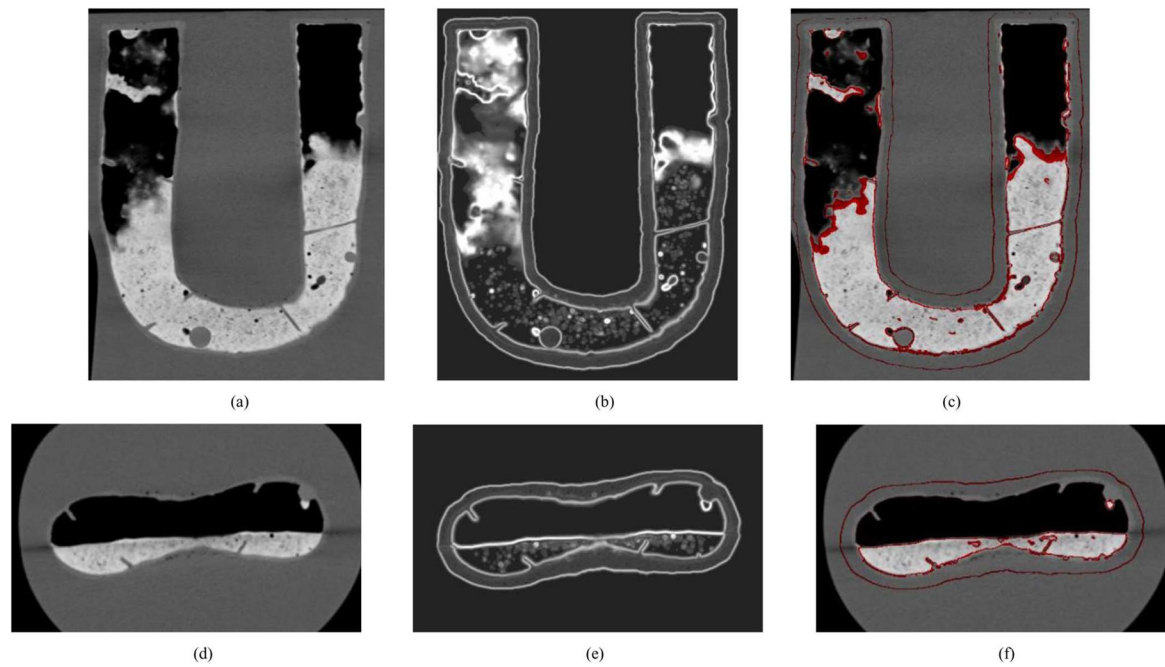


Fig. 7. Decomposition of CTC images of the fecal-tagging phantom. (a), (d): Coronal (a) and axial (d) CTC images of the fecal-tagging phantom. (b), (e): The gradient images of (a), (d), respectively, which demonstrate the inhomogeneity of the tagged materials. (c), (f): The decomposed tiles of (a), (d), respectively.

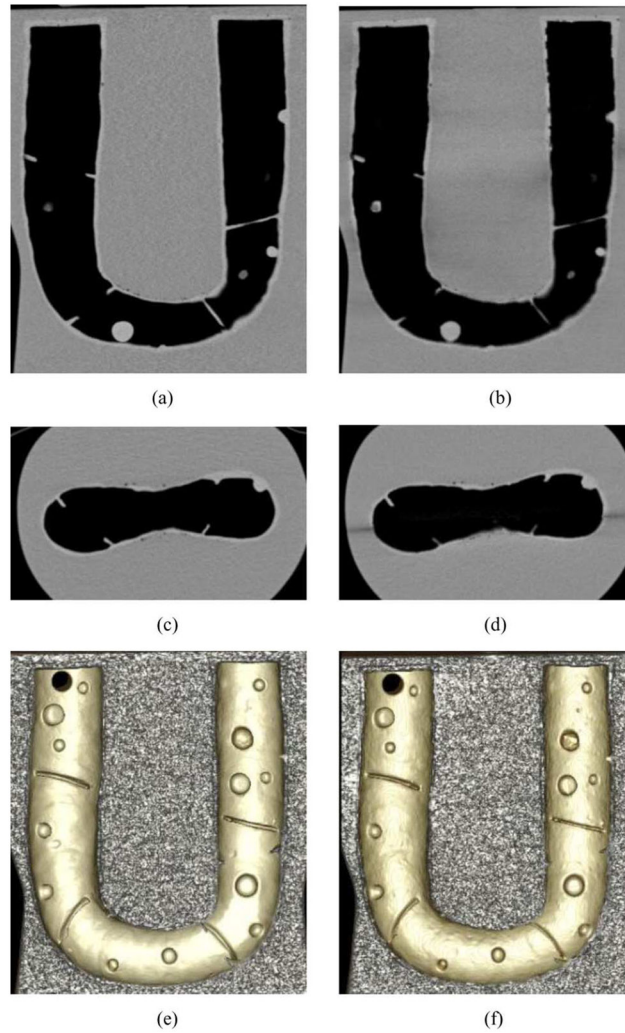


Fig. 8. Comparison between reference phantom and cleansed phantom. (a), (c): Images from the reference phantom. (b), (d) Images from cleansed phantom. The original fecal-tagging CTC images are displayed in Fig. 7(a) and (d). (e) 3-D rendered image of the reference phantom. (f) 3-D rendered image of the same region in (e) in the cleansed phantom, in which the displayed region was initially submerged in the tagged materials.

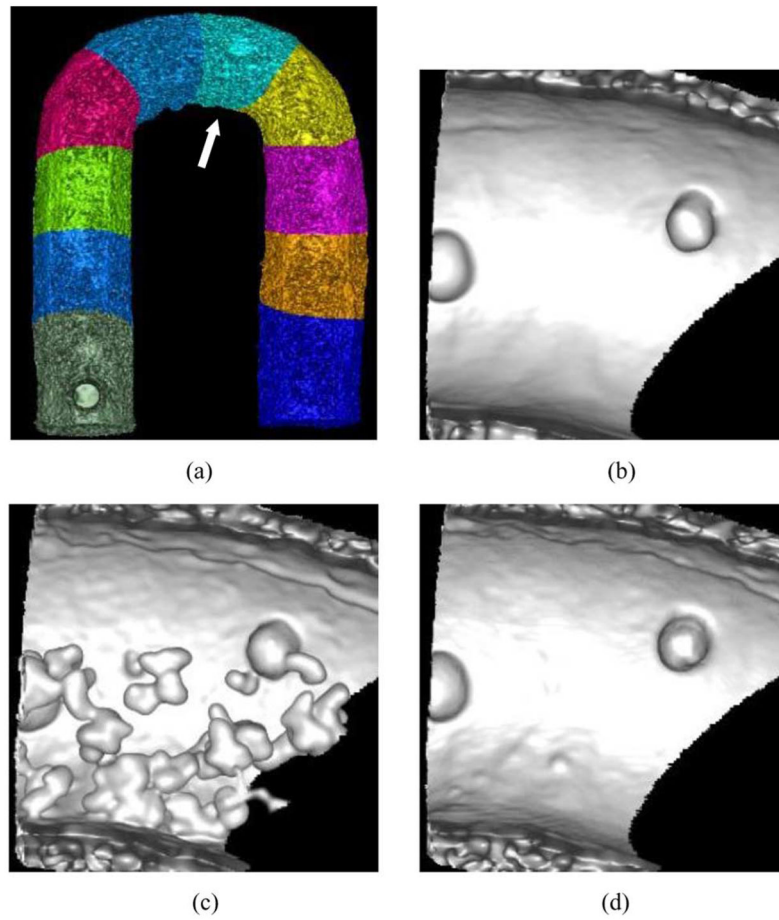


Fig. 9. Phantom evaluation of the cleansing quality. (a) The reference phantom was divided into 10 segments along its centerline. (b)–(d) 3-D-rendering image of the fifth segment [pointed out by an arrow in (a)] in the reference phantom (b), in the SA-cleansing phantom (c), and in the MD-cleansing phantom (d), respectively.

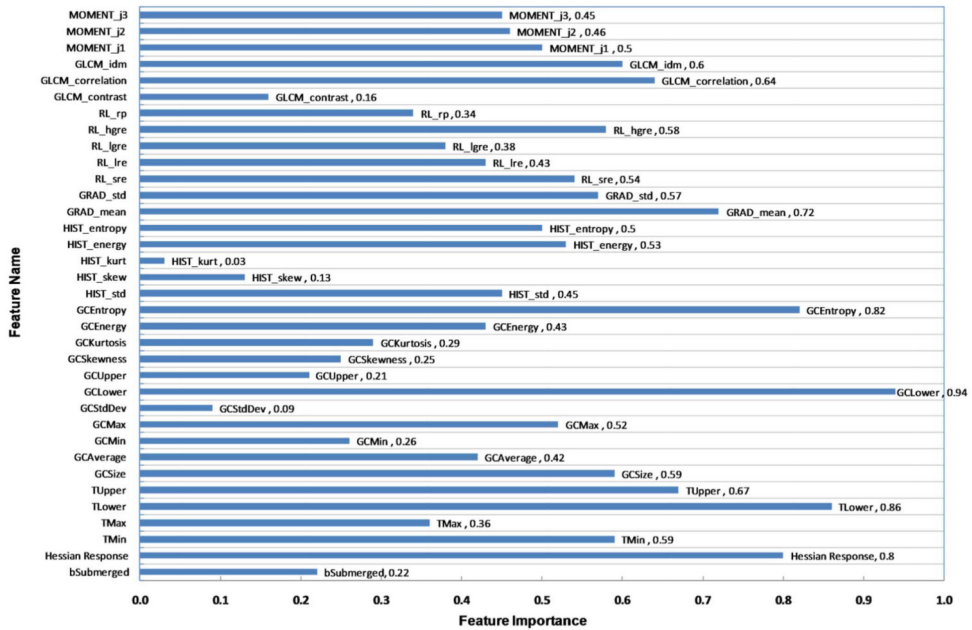


Fig. 10.

Feature importance map for soft-tissue classifier that was generated by running GA feature selection of 100 times. Each GA feature selection process was performed by a population of 10 and generations of 100. Importance value of 1.0 indicates that the associated feature was selected every time, whereas 0.0 indicates that it was never selected.

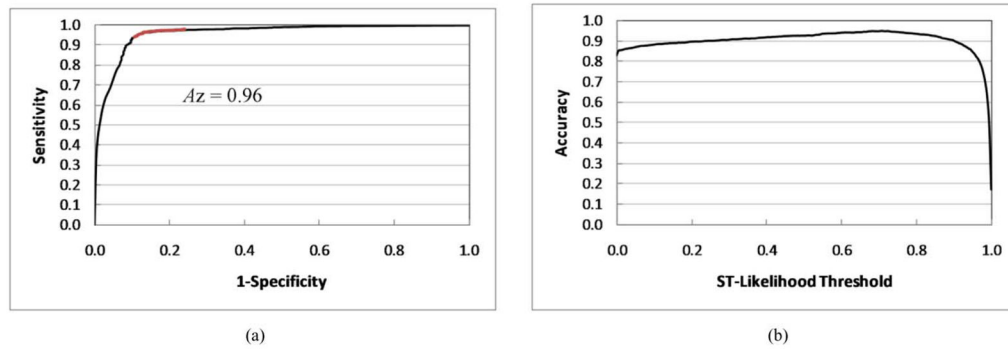


Fig. 11.

A threshold of soft-tissue likelihood was used for classifying tiles. (a) ROC curve indicates the overall performance of the SVM classifier for soft-tissue. The area under the ROC curve (A_z) was 0.96. The range of the soft-tissue likelihood between 0.6 and 0.8 is marked in red. At the operating point of 0.7, the sensitivity and specificity were 97.1% and 85.3%, respectively. (b) The accuracy $[(TP + TN)/(\text{total number of tiles})]$ curve of the SVM classifier indicates the accuracy of the SVM classifier by use of different thresholds of the soft-tissue likelihood. The accuracy was 94.7% at the operating point of 0.7.

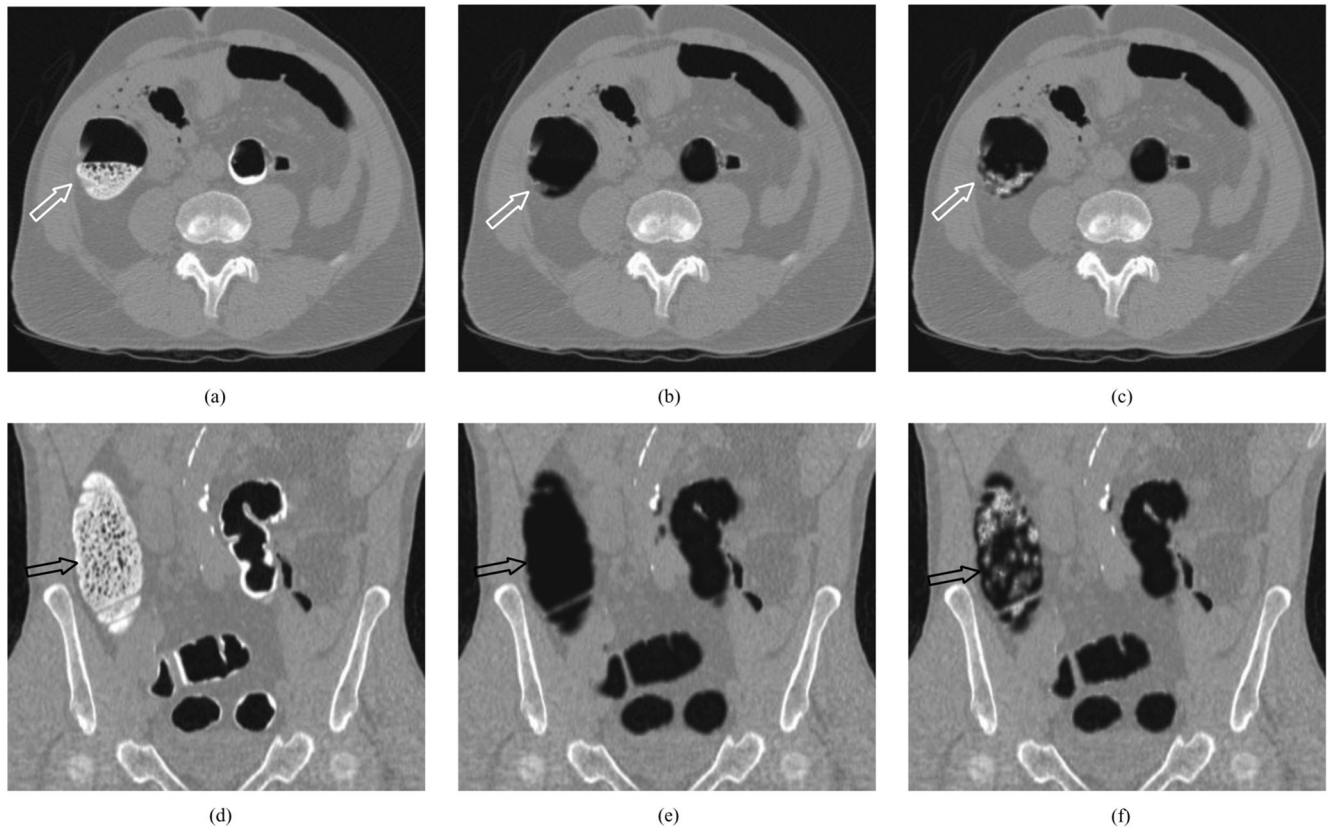


Fig. 12. Illustration of the reduction of the incomplete cleansing artifact. (a) A thin haustral fold (white arrow) is submerged in the inhomogeneously tagged stool in an axial CTC image. (b) The thin fold in (a) is preserved in MD-cleansing while the inhomogeneously tagged stool was removed. (c) The thin fold was still submerged in the incompletely cleansed fecal materials after the application of SA-cleansing. (d) Air bubbles (black arrow) were mixed with the inhomogeneously tagged stool in a coronal CTC image. (e) Air bubbles were completely cleansed after the application of MD-cleansing. (f) Air bubbles and tagged stool were incompletely cleansed after the application of SA-cleansing.

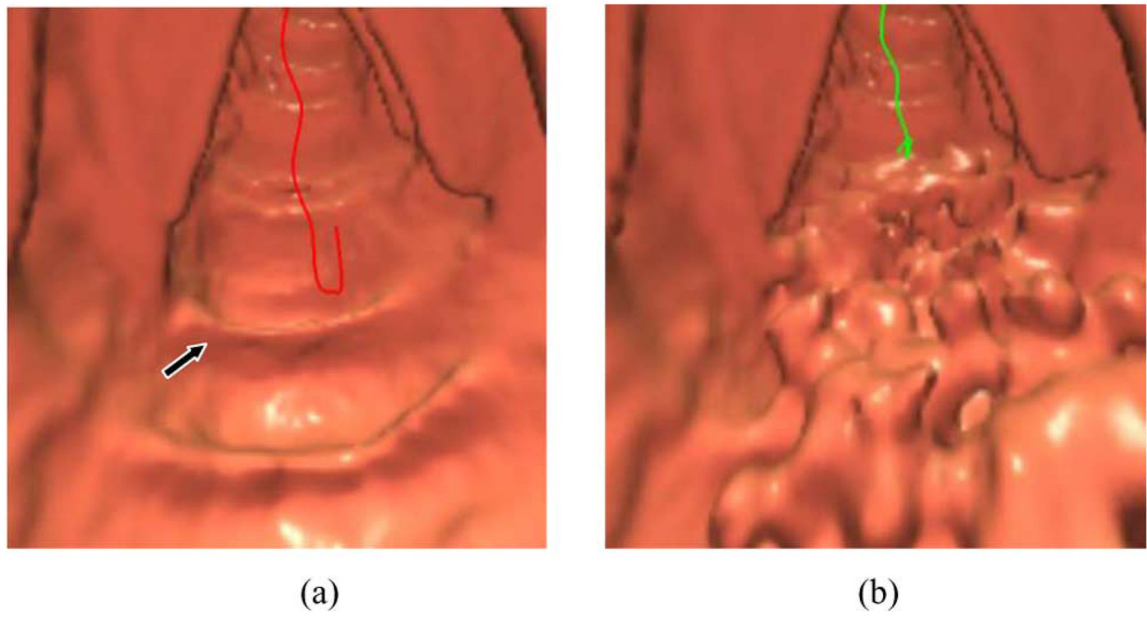


Fig. 13. Illustration of the reduction of the incomplete cleansing artifact in a 3-D endoluminal view. (a) A thin submerged fold, indicated by the arrow in Fig. 12(a), is clearly visualized after MD-cleansing. (b) The thin fold is invisible because of the obstruction of incomplete cleansing artifacts generated by SA-cleansing.

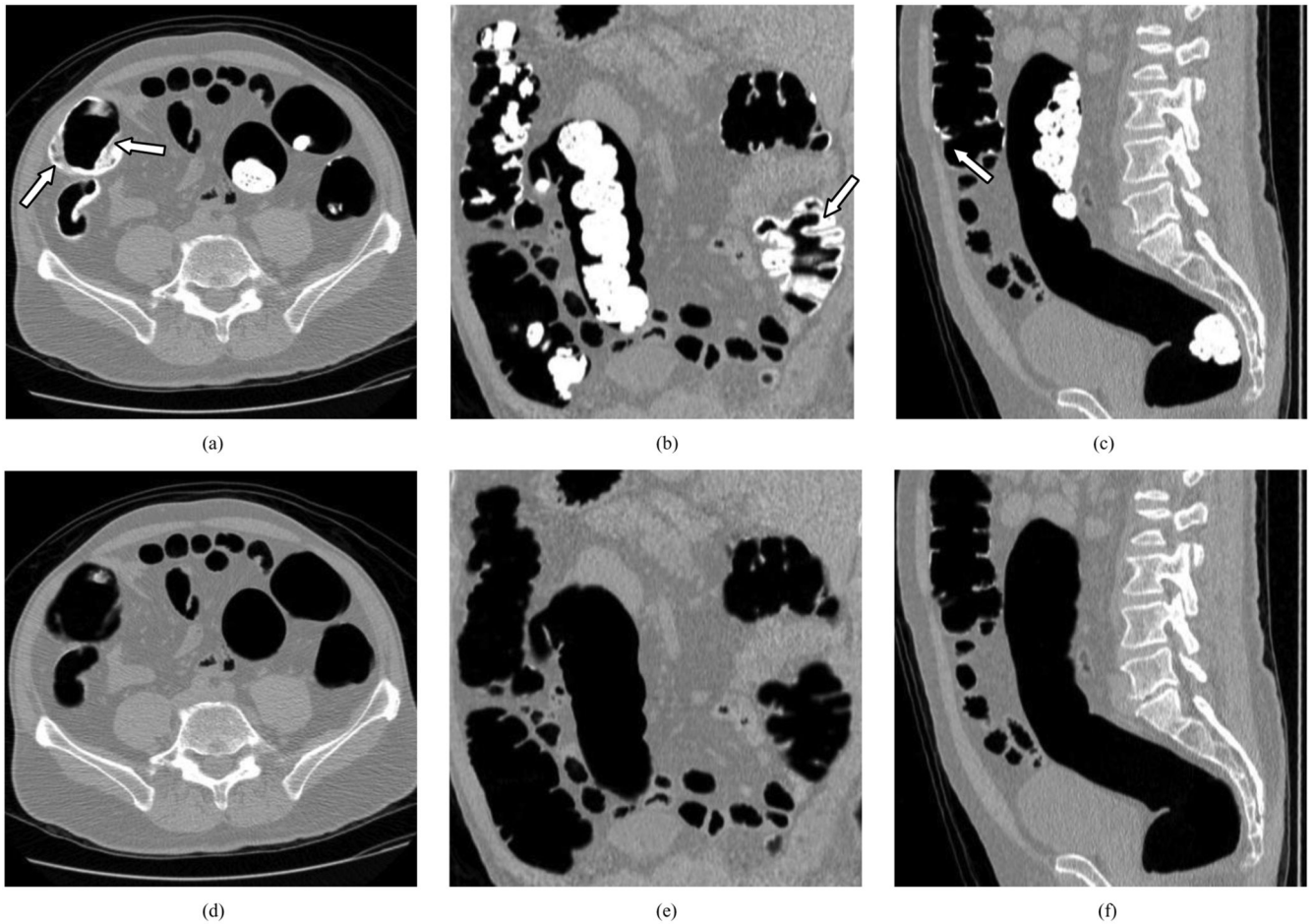


Fig. 14. Examples of the cleansing of inhomogeneously tagged fecal materials in MD-cleansing. (a)–(c) Original non-cathartic CTC images with semi-solid, inhomogeneously tagged stool. (d)–(f) Images after the application of MD-cleansing to the CTC images in (a)–(c). MD-cleansing cleans the inhomogeneously tagged fecal materials while it preserves submerged folds (white arrows).

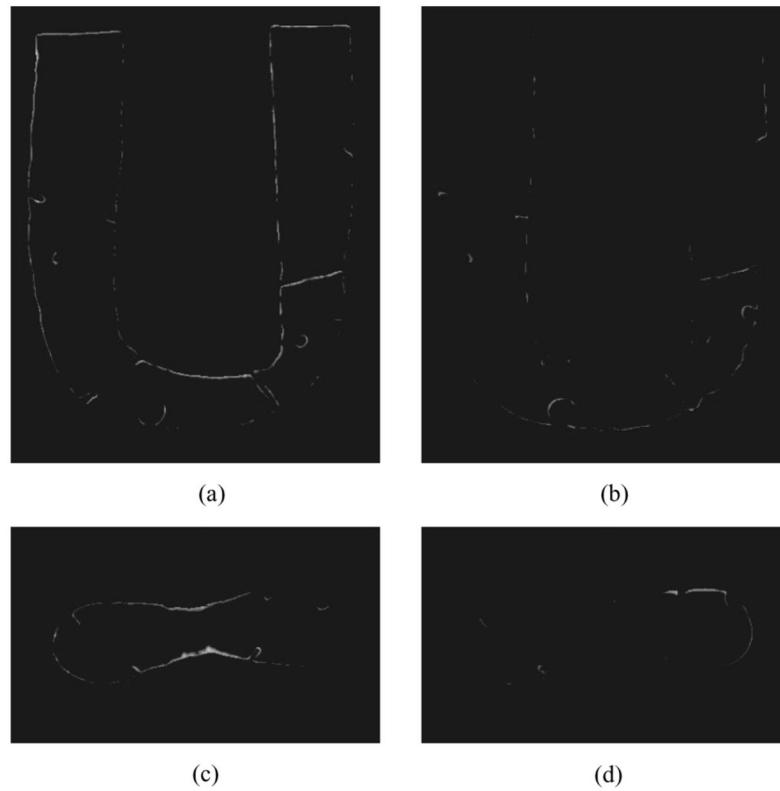


Fig. 15. Comparison between reference images and MD-cleansed images. (a), (c) Difference images from the air mask, which indicates the uncleansed portion. (b), (d) Difference images from the soft-tissue mask, which indicates the over-cleansed soft-tissue portion. The original fecal-tagging CTC images are displayed in Fig. 7(a) and (d). The cleansed images are displayed in Fig. 8(b) and (d).

TABLE I

Eigenvalue Signatures of Fold and Polyp Submerged in the Tagged Regions. Let the Eigenvalues of a Hessian Matrix H be λ_1, λ_2 , and λ_3 ($|\lambda_1| \geq |\lambda_2| \geq |\lambda_3|$), and Let Their Corresponding Eigenvectors be e_1, e_2 , and e_3 , Respectively

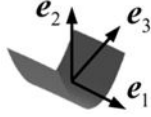
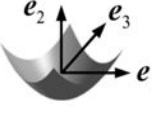
Anatomic Structure	Eigenvalue Signature	Enhancement Function
Submerged fold (Rut) 	$\lambda_3 > 0, \lambda_1 \approx 0$, and $\lambda_2 \ll \lambda_3$	$F_{rut} = \exp \left[-\frac{\left(\frac{\lambda_1}{\sqrt{ \lambda_2 \lambda_3 }} \right)^2}{2\alpha^2} \right] \cdot \exp \left[-\frac{\left(\frac{ \lambda_2 }{\lambda_3} -\gamma \right)^2}{2\beta^2} \right]$
Submerged polyp (Cup) 	$\lambda_3 > 0, \lambda_1 \approx \lambda_2$, and $\lambda_2 < \lambda_3$	$F_{cup} = F_c(\lambda_1, \lambda_2) \cdot F_c(\lambda_2, \lambda_3);$ $F_c(\lambda_i, \lambda_j) = 1 - \exp \left[-\frac{\left(\frac{\lambda_i}{\lambda_j} \right)^2}{2\eta^2} \right]$ where

TABLE II

Parameters Used for Feature Selection and Material Classification

	Name of Parameter	Value of Parameter
GA Method	Number of population	10
	Number of iteration	100
	Cross-over type	2 points
	Mutation probability	10%
SVM Classifier	SVM type	C_SVM
	Kernel type	RBF (radial basis function)
	γ (gamma)	0.15
	Cost	20

Author Manuscript

Author Manuscript

Author Manuscript

Author Manuscript

TABLE III

Comparison of MD-Cleansing and SA-cleansing in the Phantom Experiment

	Cleansing Ratio (Mean \pm Std deviation)	Soft-tissue Preservation Ratio (Mean \pm Std deviation)
SA-Cleansing	77.1 \pm 6.6 %	99.0 \pm 1.1 %
MD-Cleansing	90.6 \pm 5.1 %	97.6 \pm 1.6 %

Author Manuscript

Author Manuscript

Author Manuscript

Author Manuscript

TABLE IV

Optimal Feature Set Selected by GA for The SVM Classifier of Soft-Tissue

Feature	Feature Name
bSubmerged	Submerged boundary
TMin	Minimum value
TLower	Lower value
GCSize	Size of the core
GCLower	Lower value in core
GCEntropy	Entropy in core
HIST_std	Standard deviation of histogram
HIST_skew	Skewness of histogram
HIST_energy	Energy of histogram
HIST_entropy	Entropy of histogram
RL_sre	Short-run emphasis
RL_lre	Long-run emphasis

Author Manuscript

Author Manuscript

Author Manuscript

Author Manuscript